Journal of Marine Science and Technology

Volume 28 | Issue 6 Article 1

Experimental and Numerical Investigations on the Hydrodynamic Characteristics of the Planar Motion of an Open-Frame Remotely Operated Vehicle

Ying-fei Zan
College of Shipbuilding Engineering, Harbin Engineering University, Harbin, China

Rui-nan Guo
College of Shipbuilding Engineering, Harbin Engineering University, Harbin, China

Li-hao Yuan
College of Shipbuilding Engineering, Harbin Engineering University, Harbin, China, yuanlihao@hrbeu.edu.cn

Shi-peng Wang
College of Shipbuilding Engineering, Harbin Engineering University, Harbin, China

Da-zhong Zhang
College of Shipbuilding Engineering, Harbin Engineering University, Harbin, China

See next page for additional authors

Experimental and Numerical Investigations on the Hydrodynamic Characteristics of the Planar Motion of an Open-Frame Remotely Operated Vehicle

Acknowledgements

This research was funded by the National Key R&D Program of China (Grant No. 2018YFC0309400), Heilongjiang Province Postdoctoral Foundation of China (Grant No. LBHZ19055), and National Science and Technology Major Project of China (Grant No. 2016ZX05057020). The authors thank Chiahsing Liu at SIEMENS for his technical support in setting up the simulation.

Authors

Ying-fei Zan, Rui-nan Guo, Li-hao Yuan, Shi-peng Wang, Da-zhong Zhang, Shi-jing Xu, and Zhao-hui Wu

Journal of Marine Science and Technology, Vol. 28, No. 6, pp. 471-479 (2020)
DOI: 10.6119/JMST.202012_28(6).0001

EXPERIMENTAL AND NUMERICAL INVESTIGATIONS ON THE HYDRODYNAMIC CHARACTERISTICS OF THE PLANAR MOTION OF AN OPEN-FRAME REMOTELY OPERATED VEHICLE

Ying-fei Zan[1], Rui-nan Guo[1], Li-hao Yuan[1], Shi-peng Wang[1], Da-zhong Zhang[1], Shi-jing Xu[1], and Zhao-hui Wu[2]

Key words: remotely operated vehicle, scaled model test, hydrodynamic forces, large drift angle motion.

ABSTRACT

In this study, the longitudinal, sideways, vertical, and sideslip motions of an open-frame remotely operated vehicle (ROV) were experimentally and numerically investigated. The open-frame ROV was designed to be asymmetric in both the longitudinal and vertical directions to achieve special functionalities. A physical ROV model was tested in a towing tank with different velocities and sideslip angles in the horizontal and vertical planes. A numerical simulation was conducted with the same working conditions used in the scaled model tests by using a segregated flow solver based on Reynolds-averaged Navier–Stokes equations. This study investigated the effect of the hydrodynamic forces (moments) of other degrees of freedom (DOFs) when the open-frame ROV moved with one or two DOFs. The numerical results agreed with the experimental data. The experimental and numerical data revealed the presence of additional hydrodynamic forces attributable solely to the asymmetric structure of the open-frame ROV when the ROV moved with one or two DOFs. Accordingly, we used the numerical method to supplement an oblique towing test with large sideslip angles. The asymmetric structure had also a nonlinear effect on the hydrodynamic forces (moments), especially for large sideslip angles.

Paper submitted 11/27/19; revised 02/07/20; accepted 07/03/20. Corresponding Author: Li-hao Yuan (e-mail: yuanlihao@hrbeu.edu.cn)
[1] College of Shipbuilding Engineering, Harbin Engineering University, Harbin, China
[2] Offshore Oil Engineering Co., Ltd., Tianjin, China.

I. INTRODUCTION

Underwater vehicles, such as remotely operated vehicles (ROVs) and autonomous underwater vehicles (AUVs), are essential for the exploration of marine resources, ocean research, and the inspection and repair of undersea structures (Christ and Wernli, 2014; Khojasteh and Kamali, 2017). Bodi et al. (2015) used a swarm of AUVs for underwater exploration. Kumar et al. (2018) used AUVs to automatically track marine animals. Fluid environments, such as strong ocean currents, considerably affect the reliability and condition of AUV systems (Zheng et al., 2019). For the exploration of high depths, ROVs, which are unmanned and generally move at low speeds, are more suitable than AUVs. However, the efficient operation of ROVs requires a complete control system based on a hydrodynamic model. Hydrodynamic and hydrostatic forces are important parts of a hydrodynamic model and are mainly measured using three methods, namely the experimental, system identification (SI), and computational fluid dynamics (CFD) methods.

The experimental method requires a reduced scale model and special equipment (Fan et al., 2012a) and is the most widely used method for measuring hydrodynamic and hydrostatic forces. To measure the hydrodynamic forces of a ROV, two methods can be employed: (i) perform the uniform rectilinear motion of a ROV in a water tank to evaluate the damping forces; (ii) conduct a planar motion mechanism (PMM) test to measure inertial forces. Perez et al. (2018) proposed a mathematical model to evaluate the forces and moments experienced by an overtaking vessel due to the presence of the overtaken vessel. The SI method requires a reduced scale model with working propellers, on-board sensors, and the control signals of thrusters. On-board sensors are easily influenced by the motor and magnetic fields. It is worth noting that, although

Table 1. Parameters of the test model.

Physical property	Unit	Value
Scale ratio (λ)	/	1:4
Length (L)	m	0.875
Width (B)	m	0.5
Height (H)	m	0.5
Mass in air (W)	kg	78

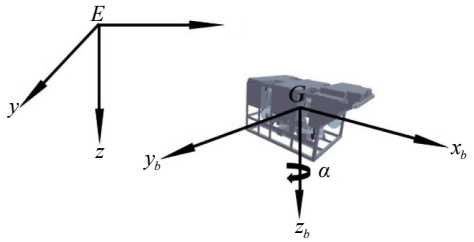

Fig. 1. Illustration of the two coordinate systems

the absence of an accelerometer in the SI method leads to a lower experimental error, which is advantageous, it also leads to a lower sampling rate, which is disadvantageous (Avila and Adamowski, 2011). Smallwood and Whitcomb (2003) used the SI method to study finite-dimensional nonlinear dynamical models for open-frame ROVs. They used a dynamical module for dynamically positioning ROVs on the basis of model-based control techniques. In the CFD method, no physical model or special equipment is required. This method only requires a computer with sufficient computing power, so it can be implemented at lower costs compared to the experimental and SI methods. Silva Costa et al. (2017) studied the stability and maneuverability of an AUV by using the OpenFOAM software. Silva et al. (2019) analyzed the effects of the torque produced by the hull–wake interaction on the maneuverability of a flat-fish-shaped AUV. They found that the effects of the aforementioned interaction appeared when fluctuating velocity fields were used instead of average constant velocity fields in the simulation. Zhang et al. (2019b) used ANSYS CFX 14.0 to investigate the resistance characteristics of a multi-AUV system, the distance between AUVs with the least resistance, and undesirable interferences at a Reynolds number (Re) of 6.14×10^6.

By approximating the submarines' horizontal and vertical surfaces as symmetric to simplify the involved hydrodynamic forces, the slow movement hypothesis had been made, which stated that the submarines cannot move abruptly or with a large oblique angle. This is not consistent with the motion and structural characteristics of open-frame ROVs. The approach of Shambhu and Ravish (2014) is used to perform a stochastic noise analysis by considering heave, pitch, and roll motions as well as the stochastic character of the circulation of ocean currents. They presented a simple uncoupled model of damping forces by assuming ROVs with front–back and top–down symmetries. In each degree of freedom (DOF) of the Fossen's model, the hydrodynamic forces are only related to the velocity in a single direction (Fossen, 1991). Accordingly, Chin and Lum (2011) measured the hydrodynamic forces of an AUV using the CFD method and considering the AUV as a slender body. Avila et al. (2013) determined the parameters of uncoupled and coupled models of open-frame underwater vehicles using the SI method and Fossen's simple model. Caccia and Veruggio (2000) used a four-DOF hydrodynamic model to control the motion of an ROV considering the longitudinal, horizontal, and vertical yaw motion. Only the hydrodynamic asymmetry caused by motions in the same DOF can be reflected by the first three equations of motion owing to the influence of other DOFs. The four-DOF hydrodynamic model can be extended to deal with the hydrodynamic forces of open-frame ROVs. Owing to the limitations of the SI method, Mai et al. (2017) used a model that only considers the uncoupled or less ordered nonlinear hydrodynamic forces. An uncoupled model can reflect the movement of an ROV only if the ROV has a symmetrical structure, and a coupled model does not consider vertical hydrodynamic forces. Based on Fossen and Caccia's theory, Suzuki et al. (2013) developed a model that considers the damping forces as well as the codirectional and angular velocities. They also measured the hydrodynamic forces of an AUV called PICASSO by using the CFD method in the model. Ramírez-Macías et al. (2016) computed the hydrodynamic forces for an ROV by using a six-DOF model. In this model, coupling terms for different velocities are obtained through the CFD method. Li et al. (2017) used the CFD method and the drag and oblique towing test to model the influence of walls on the operation of complex-shaped underwater robots according to a five-DOF coupled model. Only draft angles below 10° were considered in the model. More accurate methods have been used to describe the motion of ROVs. Xu et al. (2015) used vertical towing tests to examine an asymmetrical ROV. The longitudinal and vertical forces and moments of trim as well as their coefficients in one DOF were determined. Fan et al. (2012b) presented a five-DOF model and measured the hydrodynamics of a deep-sea operational ROV through vertical planar motion mechanism and large amplitude plane motion mechanism towing tests. In their research, the coupled and nonlinear hydrodynamics under different DOFs were investigated; however, only the lateral force and yaw moment were determined in the oblique test with a large draft angle.

In this study, drag and oblique towing tests as well as the CFD method were used to obtain a large amount of reference data for the high maneuverability operation of ROVs, especially for the oblique motion at various longitudinal speeds with a large draft angle, and to study the coupled hydrodynamic forces in the horizontal plane. The drag and oblique towing tests were conducted with an ROV module at Harbin Engineering University. Then, numerical simulations were performed using STAR-CCM+ 13.04 CFD software (Berlin,

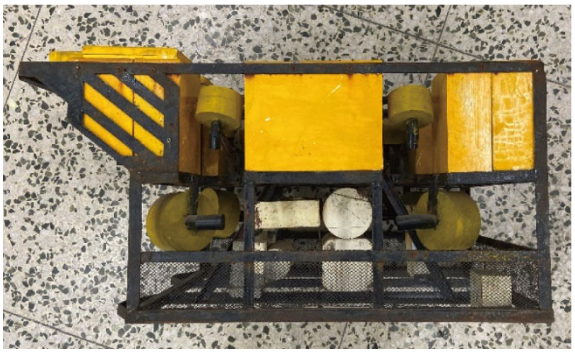

Fig. 2. Photograph of the test model.

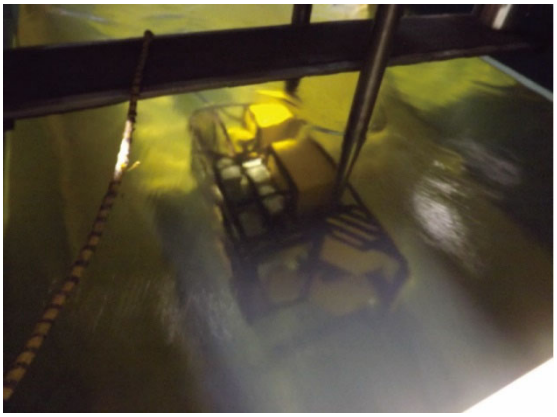

Fig. 3. Photograph of a test module in the water tank.

Germany), and the numerical results were compared with the experiment data. The main objective was to acquire insights regarding the asymmetric and nonlinear effects of hydrodynamic forces (moments) of other DOFs when the open-frame ROV moved with one or two DOFs.

II. EXPERIMENTAL STUDY

1. Description of the Coordinate System

In this study, two coordinate systems (Fig. 1) were established according to the terminology bulletin system recommended by the International Towing Tank Conference and Society of Naval Architects and Marine Engineers. The first coordinate system is the North-East-Down coordinate system, whose origin E is defined relative to the Earth's reference ellipsoid. In this system, the x-, y-, and z-axes point toward the true north, toward the east, and downward normal to the Earth's surface, respectively. The second coordinate system adopted is the body-fixed coordinate system, whose origin G is a moving coordinate frame fixed to the center of gravity of the ROV. In this system, x_b is the longitudinal axis (extending from aft to fore), y_b is the transversal axis (directed toward starboard), and z_b is the normal axis (extending from top to bottom).

Table 2. Test conditions.

	Test type	Direction	Conditions
1DOF motion	Longitudinal tests	$\pm Gx_b$	The current speed is changed from 0.3 to 0.8 m/s at 0.05 m/s intervals.
	Vertical tests	$\pm Gz_b$	The velocity of the ROV is changed from 0.25 to 0.55 m/s at 0.05 m/s intervals.
	Sideslip tests	$\pm Gy_b$	The current speed is changed from 0.25 to 0.55 m/s at 0.05 m/s intervals.
2DOF motion	Oblique towing tests	Gx_by_b	The current speed is changed from 0.55 to 0.75 m/s at 0.1 m/s intervals; the drift angle is changed from ±2° to ±10° at 1° intervals.

2. Geometry and General Parameters

The frame structure of the ROV was made of steel, and the other components within the frame were made of buoyant material (Fig. 2). The test model was front–rear and top–bottom asymmetrical, and its scale ratio was 1:4. The general ROV parameters are listed in Table 1.

3. Experiment Setup

The scale model tests were performed at Harbin Engineering University. The longitudinal towing test was completed in a 1.7 m wide and 1.5 m deep circulating water tank. The maximum speed of the circulating water was 1.0 m/s. During the experiment, the experimental model was fixed in the tank with its x-axis parallel to the flow direction. The flow moved forward and backward relative to the model at a constant velocity. The vertical direct experiments were conducted in a large water tank that was 50 m long, 30 m wide, and 10 m deep. In these experiments, the water was still and the model was connected with an XY carriage through a connecting rod, which restricted the movement of the model in the left, right, upward, and downward directions to a constant speed. In all the direct experiments, the relative velocity between the fluid and the experimental model changed within a certain range, and the experimental results at each speed were measured repeatedly. In the model test, the ROV was fixed on the PMM. The mechanism and ROV were connected by a six-DOF force transducer at the center of gravity of the ROV. Fig. 3 shows a photograph of a test module in the water tank.

The oblique experiment was conducted in the circulating tank. The experimental model was fixed in the tank with a certain drift angle. The hydrodynamic forces (moments) of the model were measured by changing the angle and velocity of

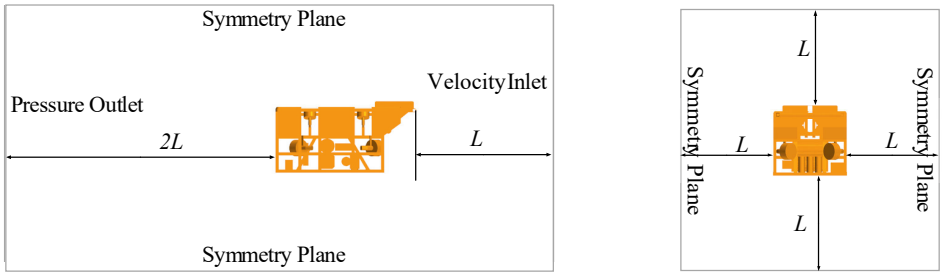

Fig. 4. Boundary conditions in the numerical simulation.

the flow. Under each experimental condition, the force of the model was measured repeatedly.

4. Test Conditions

In this study, only the damping forces and moments on the test model had to be investigated. Therefore, only the longitudinal, sideslip, vertical, and oblique towing tests were performed. The test conditions are listed in Table 2. The conditions were repeated nine times, and the resultant data wereanalyzed to determine the asymmetric effect of the ROV. Different velocities of longitudinal and vertical motion were tested to investigate the nonlinear effect of the ROV. The different velocities were tested with a series of drift angles, on both the port and starboard sides.

III. NUMERICAL STUDY

1. Governing Equations

The numerical simulations were performed with the STAR-CCM+13.04 CFD software (Berlin, Germany). The governing equations were modeled using the Reynolds-averaged Navier–Stokes equation (RANS):

$$\frac{\partial \rho}{\partial t}+\nabla\left(\rho\bar{\mathbf{v}}\right)=0 \tag{1}$$

$$\frac{\partial}{\partial t}\left(\rho\bar{\mathbf{v}}\right)+\nabla\left(\rho\bar{\mathbf{v}}\otimes\bar{\mathbf{v}}\right)=-\nabla\bar{p}\mathbf{I}+\nabla\left(\mathbf{T}+\mathbf{T}_t\right)+\mathbf{f}_\mathrm{b} \tag{2}$$

where ρ is the fluid density, $\bar{\mathbf{v}}$ and $\bar{p}$ are the mean velocity and pressure, respectively, $\mathbf{I}$ is the identity tensor, $\mathbf{T}$ is the viscous stress tensor, $\mathbf{f}_\mathrm{b}$ is the resultant of the body force, and $\mathbf{T}_t$ is the Reynolds stress tensor.

The finite volume method was employed to discretize the governing equations using the segregated flow solver. The selected $k-\varepsilon$ model is a two-equation model that solves transport equations for the turbulent kinetic energy k and turbulent dissipation rate ε to determine the turbulent eddy viscosity.

The specific equations of the model are as follows:

$$\frac{\partial}{\partial t}\left(\rho k\right)+\nabla\cdot\left(\rho k\bar{\mathbf{v}}\right)=\nabla\cdot\left[\left(\mu+\frac{\mu_t}{\sigma_k}\right)\nabla k\right]+P_k-\rho\left(\varepsilon-\varepsilon_0\right)+S_k, \tag{3}$$

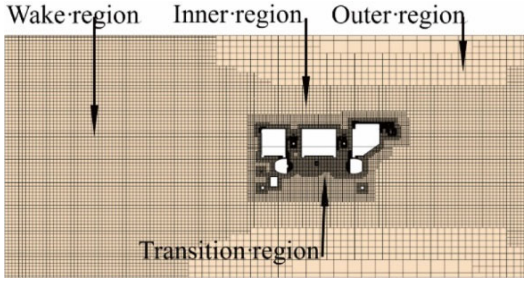

Fig. 5. Mesh arrangement for the ROV model.

$$\frac{\partial}{\partial t}\left(\rho\varepsilon\right)+\nabla\cdot\left(\rho\varepsilon\bar{\mathbf{v}}\right)=\nabla\left[\left(\mu+\frac{\mu_t}{\sigma_\varepsilon}\right)\nabla\right]+\frac{1}{T_e}C_{\varepsilon 1}P_\varepsilon-C_{\varepsilon 2}f_2\rho\left(\frac{\varepsilon}{T_e}-\frac{\varepsilon_0}{T_0}\right)+S_\varepsilon, \tag{4}$$

where μ is the dynamic viscosity; σ_k, σ_ε, $C_{\varepsilon 1}$, and $C_{\varepsilon 2}$ are model coefficients; and P_ε and P_k represent production terms. The damping function is represented by f_2, and S_k and S_ε are user-specified source terms. The large-eddy timescale is represented as follows: $T_e=k/\varepsilon$. The relationship between the specific timescale T_0, model coefficient C_t, kinematic viscosity ν, and ambient turbulence value ε_0 is defined as follows:

$$T_0=\max\left(\frac{k_0}{\varepsilon_0},C_t\sqrt{\frac{\nu}{\varepsilon_0}}\right). \tag{5}$$

2. Boundary and Simulation Conditions

The boundary conditions around the ROV model were as follows. The velocity inlet boundary was positioned at a distance 1L from the model (Jiang et al., 2017). The pressure outlet was located at a distance 2L downstream. Four symmetry plane boundaries were set at a distance 1L away from the center of gravity of the ROV. Fig. 4 illustrates the boundary conditions in the numerical simulation.

The test conditions in the simulations were supplementary to the experimental conditions. The flow speed and oblique angle of the horizontal plane are changed from 0.55 to 0.75 m/s and from ±15° to ±45° at 0.1 m/s and 5° intervals.

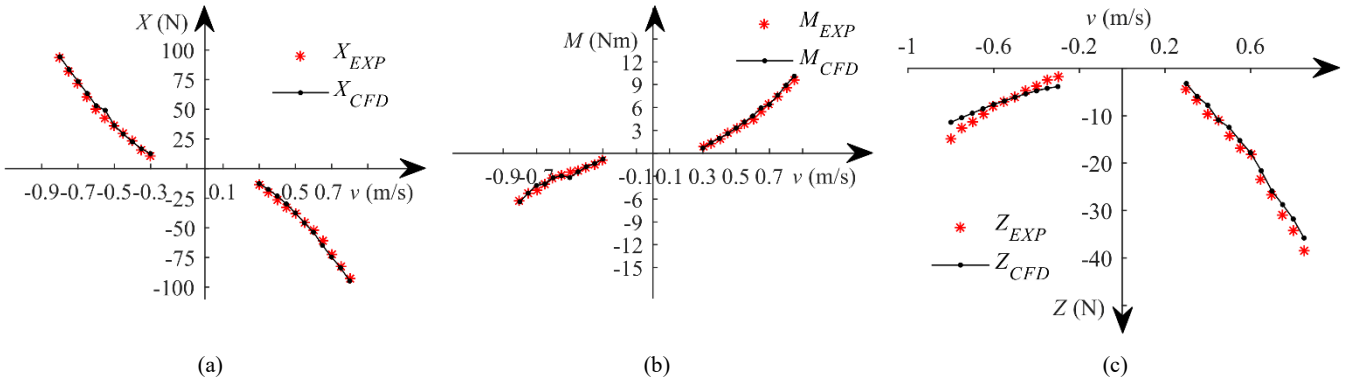

Fig. 6. Numerical and experimental results of the (a) longitudinal force X, (b) moment along the Gy_b axis M, and (c) vertical force Z.

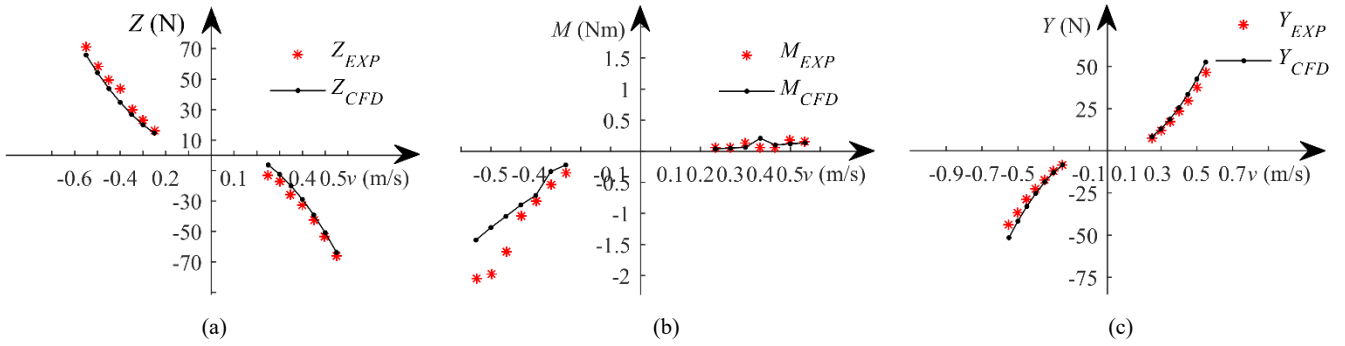

Fig. 7. Numerical and experimental results of the (a) vertical hydrodynamic force Z and (b) moment along the Gy_b axis M. (c) Numerical and sideslip test results of the lateral force Y.

3. Mesh Definition

To reflect the flow around the ROV, the fluid domain was defined by four regions: an outer region, an inner region, a wake region, and a transition region. The inner and wake regions were adopted to describe the vorticity of the flow fields in detail, and a trimmed cell mesh was used. The mesh in the outer region was coarser than the meshes in other regions and gradually transitioned into the inner region. The inner region contained the ROV, even with a draft angle, and the entire fluid region for describing the fluid surrounding the ROV. The wake region was remeshed with a grid size equal to that of the inner region, i.e., L/40. The mesh arrangement for the ROV model is illustrated in Fig. 5. The mesh size of the hull surface and the growth rate were adjusted to maintain the wall y+ values in an acceptable range (30–300) (Sezen et al., 2018). The average wall y+ value of the ROV was between 37 and 91 for all the advance coefficients.

IV. RESULTS AND DISCUSSION

1. Validation of the Longitudinal Numerical Simulations

In Figs. 6–8, the subscripts EXP and CFD denote the experimental and numerical results, respectively. Fig. 6 shows a comparison of the calculated hydrodynamic forces, namely the longitudinal force (X), vertical force (Z), and moment along the Gy_b axis (M), with the experimental results from the longitudinal tests. The numerical results reported in Sections IV.1 and IV.2 were verified by comparing them with the experimental results of Xu et al. (2015).

From Fig. 6a, it can be seen that the longitudinal force (X) increases nonlinearly in both $\pm Gx_b$ directions, and the discrepancy between X_{EXP} and X_{CFD} is mostly less than 8% in the $+Gx_b$ direction. Larger errors are observed at towing speeds of 0.35 m/s (10.9%) and 0.40 m/s (12.9%); however, the absolute errors are less than 4 N. In the $-Gx_b$ direction, the difference between X_{EXP} and X_{CFD} is less than 5.2% in most cases. Larger errors are observed at towing speeds of 0.3 m/s (23.8%) and 0.55 m/s (14.5%); however, the absolute errors are less than 7 N. The X_{CFD} values in the $+Gx_b$ and $-Gx_b$ directions are close. The maximum and minimum relative errors are 7.2% and 0.28%, respectively. These results indicate that the asymmetric characteristics of the ROV have little effect on the longitudinal force during longitudinal motion. From Fig. 6b, it can be seen that the maximum discrepancy between M_{EXP} and M_{CFD} at a towing speed of 0.3 m/s is 17.3%; however, the absolute difference is only 0.142 Nm.

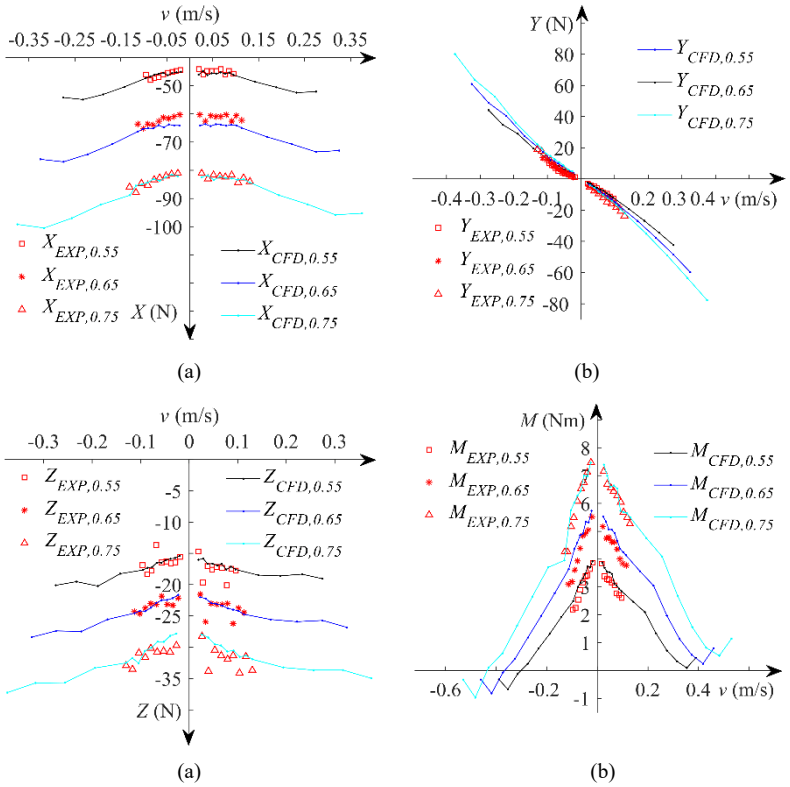

Fig. 8. Numerical and experimental results of the (a) longitudinal force X, (b) lateral force Y, (c) vertical force Z, and (d) moment along the Gy_b axis M.

M_{CFD} exhibits asymmetric characteristics. The maximum and minimum discrepancies in the M_{CFD} values are 28% and 3.9%, respectively. The M_{CFD} values in the $-Gx_b$ direction are lower than those in the $+Gx_b$ direction, except at a towing speed of 0.3 m/s; this is because an oblique plate was present in front of the ROV, and the upper half had a greater wetted area than the lower half. It can be seen from Fig. 6c that the Z_{EXP} and Z_{CFD} values are similar in the $+Gx_b$ direction. A relatively large discrepancy is observed at 0.3 m/s; however, the maximum absolute error is as low as 1.329 N. The difference between the Z_{EXP} and Z_{CFD} values is large in the $-Gx_b$ direction, especially at speeds lower than 0.5 m/s. This difference can be largely attributed to the modeling difference between the experimental scale model and the numerical model. The maximum difference between the Z_{EXP} and Z_{CFD} values at velocities between 0.5 and 0.75 m/s is 11.4%; however, the absolute error is less than 3 N. Furthermore, Z_{EXP} and Z_{CFD} exhibit asymmetric characteristics in the $\pm Gx_b$ directions. The average difference is 83.3%. It can be concluded that the front–back and top–down asymmetric characteristics of the ROV have a considerable effect on the vertical force and moment along the Gy_b axis.

2. Validation of the Vertical and Sideslip Numerical Simulations

Fig. 7 shows a comparison of the simulation and experimental results of the vertical hydrodynamic force Z and moment along the Gy_b axis M from the vertical test results as well as the lateral force Y from the sideslip test results. As can be seen in Fig. 7a, the vertical hydrodynamic force (Z) increases nonlinearly in the vertical direction. The difference between Z_{EXP} and Z_{CFD} during low-speed (below 0.35 m/s) towing is greater than that during high-speed towing, and their relative errors in the $-Gz_b$ direction are greater than 11%, owing the shape change and crevice formation in the ROV scale module. However, the maximum absolute difference is less than 7.3 N, which is considerably smaller than the buoyancy (549 N). At high speeds (above 0.4 m/s), Z_{EXP} and Z_{CFD} are symmetrical in the $\pm Gz_b$ directions The relative difference in Z_{EXP} in the two directions is less than 11%. Fig. 7b illustrates the moment along the Gy_b axis (M). The absolute errors of M are less than 0.74 Nm, and M_{CFD} exhibits asymmetric characteristics due to the front–back symmetry of the ROV. The moment M_{EXP} oscillates considerably with speed in the Gz_b direction. In those cases, the value was small; therefore, the carriage vibration or current speed instability may have caused a large uncertainty in the measured data. The module used in the simulation was not the same as the experimental module, and, because the moment is sensitive to the flow and geometry, the difference between M_{EXP} and M_{CFD} is relatively large. Fig. 7c illustrates the lateral force (Y) obtained

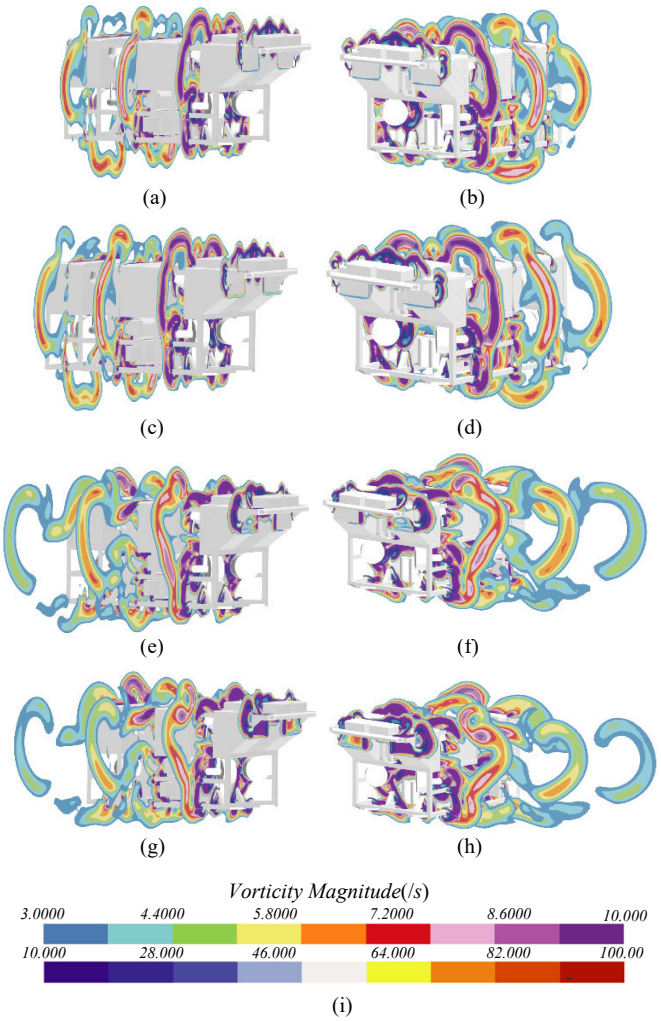

Fig. 9. Vorticity magnitude comparison in the $\pm Gy_b$ directions at α = (a) 5°, (b) −5°, (c) 10°, (d) −10°, (e) 40°, (f) −40°, (g) 45°, and (h) −45°; (i) shows the color bar representing the vorticity magnitude.

from the simulation and the sideslip tests. As shown in the Fig. 7c, the discrepancy between Y_{EXP} and Y_{CFD} is less than 15%, except at 0.55 m/s. The maximum difference in Y_{CFD} is less than 2.1%, indicating good symmetry.

The longitudinal force X, vertical force Z, lateral force Y, and moment along the Gy_b axis M were reasonably accurately predicted. Thus, the CFD solver, numerical methods, and computational grids worked well for the simulation of the ROV motion, and further analysis can be conducted based on the numerical predictions. For one-DOF motion, forces along the main DOF were symmetrical, but the forces and moments perpendicular to the main DOF were asymmetrical.

3. Results of the Oblique Tests

Fig. 8 displays a comparison of the experimental and numerical results obtained in the oblique tests at the current speeds of 0.55, 0.65, and 0.75 m/s, which are varied with lateral speed, calculated as $v = U\cos\alpha$. As depicted in Fig. 8a, when the drift angle is less than 10°, the relative errors are less than 4.5% at the current speeds of 0.55 and 0.75 m/s. When the drift angle is +7°, the maximum discrepancy at 0.65 m/s is 6.5%. The force X_{CFD} changes nonlinearly to a large extent with the lateral speed. The force X_{CFD} reaches its minimum value at an α value of 40° at each current speed. The longitudinal forces are symmetrical when α is below 45°. Furthermore, the differences in the forces are lower than 3.3% when α is less than 10°. In three cases, the difference of the forces is over 5% at α = 20°.

As displayed in Fig. 8b, the current speed has a smaller effect on Y than on X. The maximum difference between the Y at the three current speeds in both drift angle is 56.1%, which is obtained at the current speed of 0.65 m/s with a drift angle of −7°. The lateral force Y increases nonlinearly with the lateral speed and does not reach its peak value when $|\alpha| < 45°$. The relative difference between the experimental and numerical data is relatively large; however, the absolute differences are less than 1.8 and 3.7 N when the drift angle is positive and negative, respectively. The lateral forces are nearly symmetrical about the origin, except at a drift angle of 12°. The differences in the forces are less than 5% when $|\alpha| > 4°$.

The differences in the vertical forces (Z) are lower than 9%, except when $\alpha = \pm 3°$ and ±8°. The maximum difference in the vertical forces is 12.1% in the horizontal plane. Thus, the vertical forces have symmetrical characteristics. The rate of increase in the vertical forces decreases when α approaches 40°, and Z increases marginally when α further increases to 45°.

Fig. 8d illustrates the results for the moments along the y-axis (M). The differences in the moments are always less than 11% when $\alpha > 0$ except when $\alpha = -7°$ and −8°. The moments are symmetrical when $|\alpha| < 8°$ because their maximum difference in this range is 6.2%. However, M becomes asymmetrical when $|\alpha| > 8°$, and the asymmetry enhances with increasing drift angle. The moment is lower than 0 when $\alpha < -35°$, and the lowest moment is observed when $\alpha = \pm 35°$.

The forces X and Z oscillated considerably with the drift angle, whereas Y and M did not. The carriage vibration and current speed instability influenced the aforementioned oscillations; however, the main reason for the oscillations was the flow field variation. The complex structure of the ROV induced numerous vortices that caused the oscillations of forces and moments. Furthermore, the ROV was more asymmetrical in the longitudinal and vertical directions than in the horizontal direction. Therefore, the flow field was more complex in the longitudinal and vertical directions. Consequently, X and Z oscillated to a considerably greater extent than Y and M.

During the oblique motion along the Gx_b and Gy_b axis, X and Y, which are the forces along the main DOF of motion,

were nearly symmetrical in both the $\pm Gy_b$ directions. Z exhibited good symmetrical characteristics, in contrast to the one-DOF motions. M was only symmetrical at low drift angles.

4. Detailed Flow Field Analysis

Fig. 9 illustrates the cross sections of the flow field at a current speed of 0.55 m/s colored according to the vorticity magnitude. To express the flow field clearly, two color bars are used in the figures.

As displayed in Fig. 9, numerous vortices arise at the outlet section. The vortices of all the cross sections are around the ROV at low drift angles, and they separate at large drift angles. The vortices in the $\pm Gy_b$ directions are similar at the same absolute drift angle in both the vertical and horizontal planes. Therefore, the forces in the planes, i.e., the longitudinal force X, lateral force Y, and vertical force Z, are symmetrical around the origin of the coordinate axis. The vorticity magnitude in the same cross section decreases with increasing drift angle, and the planes near the stern of the ROV decrease more significantly. When the large-magnitude vortices are mainly in the $-Gx_b$ direction, the longitudinal force increases and the longitudinal velocity decreases with increasing drift angle. These results agree with those of Zhang et al. (2019). The vortices of vorticity magnitude do not follow the $-Gx_b$ direction at large drift angles, and the influence of the vortices is lower than that of the velocity. Therefore, the longitudinal force decreases. The lateral velocity increases with the drift angle; therefore, the lateral force also increases (Mabrouk et al., 2007).

In the vertical direction, a large number of high-vorticity vortices are observed at low drift angles near the top of the stern, and a large number of low-vorticity vortices are observed at high drift angles near the top of the stern of the ROV. Therefore, the rate of increase in the dynamic vertical force decreases. When $|\alpha| > 40°$, the distribution of vortices near the stern almost stop to decrease; however, the distribution increases near the top of the stern. Therefore, the dynamic vertical force increases marginally. This phenomenon also influences the moment along the Gy_b axis, which decreases partly owing to the reduction of vortices near the lower end of the stern and partly owing to the increase in vortices near the top end.

V. CONCLUSIONS

In this study, experimental and numerical methods were used to investigate the longitudinal, sideways, vertical, and sideslip motions of an ROV. First, the longitudinal, sideways, and vertical motions were simulated to validate the grid and test module. Then, oblique simulations were performed based on the obtained results. Moreover, tests were conducted for drift angles of 10°−45°. For validation purposes, the numerical predictions of the hydrodynamic forces and moments were compared with the experimental data. The comparison indicated that the CFD solver, numerical methods, and computing grids are sufficiently accurate for simulating the motion of an ROV and predicting the longitudinal force, lateral force, vertical force, and moment by trim. The analysis of the numerical data indicated that owing to the asymmetrical characteristics of the ROV, forces and moments in the direction of motion were symmetrical and those perpendicular to the direction of motion were asymmetrical in the longitudinal and vertical motion. The front–back and top–down asymmetric characteristics of the ROV had a considerable effect on the vertical force and moment by trim. However, no effect was observed on the horizontal oblique motion because the ROV was nearly symmetrical in the lateral direction. In the oblique motion, the forces and moments varied nonlinearly with the lateral velocity. Moreover, the longitudinal force and moment of trim reached their peak values at large drift angles. The forces along the main DOF of motion were nearly symmetrical in the port and starboard side. Moreover, the vertical force exhibited good symmetrical characteristics, in contrast to the one-DOF motions. Vorticity magnitude illustrations are shown to explain the reason for the variation in the forces and moments. The longitudinal force decreased at large drift angles because the vortices of vorticity magnitude did not follow the longitudinal direction. The reduction in the distribution in vortices near the lower end of the ROV stern and the increase in vortices near the top end deceased the moment by trim.

ACKNOWLEDGMENT

This research was funded by the National Key R&D Program of China (Grant No. 2018YFC0309400), Heilongjiang Province Postdoctoral Foundation of China (Grant No. LBH-Z19055), and National Science and Technology Major Project of China (Grant No. 2016ZX05057020). The authors thank Chiahsing Liu at SIEMENS for his technical support in setting up the simulation.

REFERENCES

Avila, J. P. J. and J. C. Adamowski (2011). Experimental evaluation of the hydrodynamic coefficients of a ROV through Morison's equation. Ocean Engineering 38, 2162-2170.

Avila, J. P. J., D. C. Donha and J. C. Adamowski (2013). Experimental model identification of open-frame underwater vehicles. Ocean Engineering 60, 81-94.

Bodi, M., C. Mslinger, R. Thenius and T. Schmickl (2015). BEECLUST used for exploration tasks in Autonomous Underwater Vehicles. IFAC-PapersOnLine 48, 819-824.

Caccia, M. and G. Veruggio (2000). Guidance and control of a reconfigurable unmanned underwater vehicle. Control Engineering Practice 8, 21-37.

Chin, C. S. and S.H. Lum (2011). Rapid modeling and control systems prototyping of a marine robotic vehicle with model uncertainties using xPC Target system. Ocean Engineering 38, 2128-2141.

Christ, R.D. and R.L. Wernli (2014). The ROV Manual, 2nd Edition. Butterworth-Heinemann, Oxford, 641-661.

Fan, S., L. Lian and P. Ren (2012a). Research on hydrodynamics model test for deepsea open-framed remotely operated vehicle. China Ocean Engineering 26, 329-339.

Fan, S., L. Lian, P. Ren and G. Huang (2012b). Oblique Towing Test and Maneuver Simulation at Low Speed and Large Drift Angle for Deep Sea Open-Framed Remotely Operated Vehicle. Journal of Hydrodynamics 24, 280-286.

Fossen, T. I. (1991). Nonlinear Modelling and Control of Underwater Vehicles, Department of Marine Technology. Norwegian University of Science and Technology, Trondheim, Norway.

Jiang, Y., H. Sun, J. Zou, A. Hu and J. Yang (2017). Experimental and numerical investigations on hydrodynamic and aerodynamic characteristics of the tunnel of planing trimaran. Applied Ocean Research 63, 1-10.

Khojasteh, D. and R. Kamali (2017). Design and dynamic study of a ROV with application to oil and gas industries of Persian Gulf. Ocean Engineering 136, 18-30.

Kumar, G. S., U.V. Painumgal, M. Kumar and K. Rajesh (2018). Autonomous Underwater Vehicle for Vision Based Tracking. Procedia Computer Science 133, 169-180.

Li, Z., J. Tao, H. Sun, Y. Luo, L. Ding and Z. Deng (2017). Hydrodynamic calculation and analysis of a complex-shaped underwater robot based on computational fluid dynamics and prototype test. Advances in Mechanical Engineering 9, 1-10.

Mabrouk, R., J. Chaouki and C. Guy (2007). Effective drag coefficient investigation in the acceleration zone of an upward gas–solid flow. Chemical Engineering Science 62, 318-327.

Mai, C., S. Pedersen, L. Hansen, K. Jepsen and Z. Yang (2017). Modeling and Control of Industrial ROV's for Semi-Autonomous Subsea Maintenance Services. IFAC-PapersOnLine 50, 13686-13691.

Perez, T., A. Donaire and F. Valentinis (2018). Parametric Modelling of Interacting Hydrodynamic Forces in Underwater Vehicles Operating in Close Proximity IFAC-PapersOnLine 51, 92-97.

Ramírez-Macías, J. A., P. Brongers, S. Rúa and R. E. Vásquez (2016). Hydrodynamic modelling for the remotely operated vehicle Visor3 using CFD. IFAC-PapersOnLine 49, 187-192.

Sezen, S., A. Dogrul, C. Delen and S. Bal (2018) Investigation of self-propulsion of DARPA Suboff by RANS method. Ocean Engineering 150, 258-271.

Shambhu, N. S. and H. H. Ravish (2014). An underwater vehicles dynamics in the presence of noise and Fokker-Planck equations. IFAC Proceedings 47, 8805-8811.

Silva, C.G., M.P. Almeida, A. Filho, A.T. Cunha Lima and I. C. Cunha Lima (2019). 3-D realistic simulations over a Flatfish shaped AUV submitted to ocean currents. Applied Ocean Research 90, 1-7.

Silva C., A. Ruiz, M.A. Reis, A. Lima, M.P. Almeida and I. C. Cunha Lima (2017). Numerical analysis of stability and manoeuvrability of Autonomous Underwater Vehicles (AUV) with fishtail shape. Ocean Engineering 144, 320-326.

Smallwood, D.A. and L. L. Whitcomb (2003). Adaptive identification of dynamically positioned underwater robotic vehicles. IEEE Transactions on Control Systems Technology 11, 505-515.

Suzuki, H., J. Sakaguchi, T. Inoue, Y. Watanabe and H. Yoshida (2013). Evaluation of methods to Estimate Hydrodynamic Force Coefficients of Underwater Vehicle based on CFD. IFAC Proceedings Volumes 46, 197-202.

Xu, S. J., D. F. Han and Q. W. Ma (2015). Hydrodynamic forces and moments acting on a remotely operate vehicle with an asymmetric shape moving in a vertical plane. European Journal of Mechanics - B/Fluids 54, 1-9.

Zhang, C., X. Liu, D. Wan and J. Wang (2019a). Experimental and numerical investigations of advancing speed effects on hydrodynamic derivatives in MMG model, part I: Xvv, Yv, Nv. Ocean Engineering 179, 67-75.

Zhang, D., G. Pan, Y. Shi, P. Wang and L. Chao (2019b). Investigation of the resistance characteristics of a multi-AUV system. Applied Ocean Research 89, 59-70.

Zheng, X., C. Feng, T. Li and B. He (2019). Analysis of Autonomous Underwater Vehicle (AUV) navigational states based on complex networks. Ocean Engineering 187, 1-11.